

Stable Solid-State Zinc–Iodine Batteries Enabled by an Inorganic ZnPS₃ Solid Electrolyte with Interconnected Zn²⁺ Migration Channels

Zeheng Lv, Yuanhong Kang, Guanhong Chen, Jin Yang, Minghui Chen, Pengxiang Lin, Qilong Wu, Minghao Zhang, Jinbao Zhao,* and Yang Yang*

Aqueous zinc–iodine (Zn–I₂) batteries, with their outstanding merits in safety, cost, and environmental friendliness, have received extensive attention. However, the unstable electrochemistry at the electrode–electrolyte interface originating from free water results in zinc dendrite growth, hydrogen evolution reaction (HER), and polyiodide ions shuttle, hindering their practical applications. Herein, solid-state Zn–I₂ batteries based on an inorganic ZnPS₃ (ZPS) electrolyte are developed to overcome inherent interfacial issues associated with aqueous electrolytes. The inorganic ZnPS₃ electrolyte, with a low Zn²⁺ diffusion energy barrier of ≈ 0.3 eV, demonstrates an exceptional ion conductivity of 2.0×10^{-3} S cm⁻¹ (30 °C), which also satisfies high chemical/electrochemical stability and mechanical strength. The solid Zn²⁺ conduction mechanism, facilitated by bounded water only on grains, effectively suppresses HER and polyiodide ions shuttling. During cycling, a ZnS functional layer is spontaneously formed on the anode/electrolyte interphase, promoting dendrite-free Zn deposition behavior with a more stable (002) crystal orientation. Consequently, the solid-state configuration of Zn–I₂ battery enables an impressive reversible capacity of 154.2 mAh g⁻¹ after 400 cycles at 0.1 A g⁻¹. Importantly, the compatibility of the solid-state ZnPS₃ electrolyte is also confirmed in the Zn||CuS cell, indicating its potential as a versatile platform for developing inorganic solid-state zinc-ion batteries (ZIBs).

limited Li resources present significant safety concerns and economic considerations that impede their wider adoption in certain applications.^[1] Fortunately, zinc-based battery chemistries have the potential to occupy a distinct space in the applications of wearable electronics and grid-scale energy storage because of tremendous merits of Zn, such as excellent biocompatibility, low-cost, and high volumetric capacity.^[2] Furthermore, by coupling Zn metal with redox iodine cathodes, zinc–iodine (Zn–I₂) batteries are expected to maximize the sustainability superiority owing to the relatively abundant availability (zinc constitutes approximately 0.013% of the earth's crust, while iodine is present in seawater at 55 $\mu\text{g L}^{-1}$).^[3]

Aqueous electrolytes have been widely used for zinc–iodine batteries due to the intrinsic safety features and high ionic conductivity. However, a large amount of free water at electrode/electrolyte interfaces will cause several critical issues upon cycling including: (1) hydrogen evolution reaction (HER) and byproduct accumulation on the Zn metal anode,^[4] (2) formation of polyiodide ions (I₃⁻ and I₅⁻) due to the highly

soluble ZnI₂ discharging product in water and the consequent shuttle effect,^[3b] and (3) indispensable porous separator with liquid electrolyte may direct the formation of Zn dendrites in their pores and leave “dead Zn” during stripping.^[4a] The development of solid-state electrolyte to replace conventional aqueous electrolytes is expected to address the above issues fundamentally by eliminating the presence of active water in the zinc–iodine battery system.

Various types of organic polymer, inorganic oxide, sulfide, and halide solid-state electrolytes have been extensively investigated for advanced solid-state Li batteries.^[1–5] Whereas, the pursuit of solid-state divalent Zn²⁺ conduction still remains a great challenge. Most of reported studies on solid-state Zn²⁺ conduction have focused on solid polymer electrolyte (SPE) systems,^[6] which involve zinc salts dissolved in highly flexible polymers, such as PEO (poly(ethylene oxide)). The high charge density nature of divalent Zn²⁺ should cause stronger bonding interaction with polymer chains, resulting in sluggish ion transport

1. Introduction

Lithium-ion batteries (LIBs) have dominated the conventional battery market over several decades. However, the flammable and eco-unfriendly nature of organic electrolytes, along with

Z. Lv, Y. Kang, G. Chen, J. Yang, M. Chen, P. Lin, Q. Wu, M. Zhang, J. Zhao, Y. Yang
State Key Laboratory of Physical Chemistry of Solid Surfaces
State-Province Joint Engineering Laboratory of Power Source Technology for New Energy Vehicle
Tan Kah Kee Innovation Laboratory (IKKEM)
College of Chemistry and Chemical Engineering
Xiamen University
Xiamen 361005, P. R. China
E-mail: jbzhaoy@xmu.edu.cn; yangyang419@xmu.edu.cn

The ORCID identification number(s) for the author(s) of this article can be found under <https://doi.org/10.1002/adfm.202310476>

DOI: 10.1002/adfm.202310476

through the polymer segmental motion and extremely low Zn^{2+} ion conductivities, typically around $\approx 10^{-4}$ mS cm^{-2} at room temperature.^[7] Certain modified SPEs, incorporating 1-ethyl-3-methylimidazolium tetrafluoroborate ([EMIM]BF₄) ionic liquid and polymerized amorphous solid poly(1,3-dioxolane), have been designed successfully to enhance Zn^{2+} ion conductivity effectively.^[6a,8] These modifications demonstrate good compatibility with insertion-type cathodes. However, the presence of non-polymer components and the amorphous structure may compromise the mechanical strength. Additionally, polyiodide ions may penetrate the polymer matrix due to their high polarity, leading to irreversible capacity loss.

On the other hand, freezing ZnSO_4 aqueous solution or solidifying deep eutectic solvents containing organic Zn salts also provide an alternative route for the preparation of solid-state Zn^{2+} electrolytes.^[7,9] Despite encouraging progress, the exploration of inorganic solid-state Zn^{2+} electrolytes is still in its infancy. In a recent study by See et al., it was found that Zn^{2+} can conduct in inorganic ZnPS_3 (ZPS). And exposing ZnPS_3 to environments with water vapor further enables its superionic conductivity (>0.1 mS cm^{-1}) through the vacancy-hopping mechanism.^[10] The exciting theoretical breakthrough in solid-state Zn^{2+} conduction offers valuable insights for further developing inorganic ZnPS_3 -based electrolytes. Although it has been demonstrated that the adsorbed H_2O in $\text{ZnPS}_3 \cdot x\text{H}_2\text{O}$ effectively improve Zn^{2+} conduction. However, the excess adsorption of H_2O ($x \geq 2.38$) can lead to disastrous structural change of ZnPS_3 .^[10b] Hence, a careful balance between the amount of adsorbed water and structural stability of ZnPS_3 is essential. And further systematic investigation is needed to assess the feasibility of using ZnPS_3 -based electrolyte in practical Zn-based batteries.

Herein, the surface environment of ZnPS_3 is manipulated by introducing hydrophobic polytetrafluoroethylene (PTFE), which also serves as binder to fabricate a dense electrolyte film through the scalable roll-to-roll preparation method. By incorporating a trace amount of water onto grains, the resultant inorganic ZPS electrolyte achieves an ultrahigh ion conductivity of 2.0×10^{-3} S cm^{-1} at 30 °C, while also demonstrating high chemical stability, electrochemical stability, and deformability. The as-prepared ZPS electrolyte not only inhibits Zn dendrite growth but also physically suppresses the diffusion of polyiodides in the solid-state zinc–iodine battery (Figure 1a). The effective reduction of active water in comparison to traditional aqueous zinc–iodine batteries simultaneously mitigates interface parasitic side reactions at the Zn anode side and iodine dissolution at the cathode side. Furthermore, the ZPS electrolyte also demonstrates good electrode compatibility with CuS cathode, providing a robust material platform for the development of inorganic solid-state zinc-ion batteries (ZIBs).

2. Results and Discussion

In the MPS₃ family of compounds (M = Zn, Fe, Cd, Mn, etc.), the high electronegativity of sulfide species causes local lattice polarizable distortions, enabling the transport of divalent ions.^[10a] Moreover, the stretchable P–P bond in the $[\text{P}_2\text{S}_6]^{4-}$ unit allows for structural flexibility, restraining the structural collapse of MPS₃ induced by M^{2+} ions diffusion. In the layered structure of ZPS, Zn^{2+} cations are coordinated with $[\text{P}_2\text{S}_6]^{4-}$ polyanions, forming

a distorted hexagonal network of edge-sharing Zn^{2+} octahedra (Figure 1b).^[10] In the inorganic crystalline framework of ZPS, the bond valence site energy (BVSE) method can be used to understand the interactions between adjacent atoms with opposite oxidation states.^[11] Every Zn^{2+} ion occupies the lattice site in ZPS with a given potential energy. And the site energies and bond lengths are relevant to bond valence. Their changes resulted from vacancy-mediated Zn^{2+} diffusion provide insights into the Zn^{2+} diffusion barriers and pathways in ZPS. As a result, the topology of Zn^{2+} migration paths between different Zn sites in the Zn layer and the corresponding migration barriers have been illustrated in Figure 1c,d, respectively. Based on the structural symmetry principle, two types of Zn sites are labeled as Zn_1 and Zn_2 , respectively. Zn_1 exhibits one-dimensional (1D) migration, directly moving through the octahedral edge to the neighboring Zn_1 site with a migration energy barrier of 0.263 eV. Besides, Zn_2 can migrate through the octahedral faces to Zn_1 along a two-dimensional (2D) pathway, with a slightly higher energy barrier of 0.272 eV. The considerable ions transport adaptability, abundant Zn^{2+} ion diffusion paths, and low Zn^{2+} migration energy barriers (≈ 0.3 eV) may enable the layered ZPS to exhibit fast Zn^{2+} transport kinetics.

In addition to ionic transport, the cost factor must also be considered when evaluating the practicality of solid-state electrolytes. The computing method developed by Hart et al. allows for the estimation and comparison of bulk purchase prices of chemicals based on their laboratory-scale prices, utilizing a logarithmic Equation (1):^[12]

$$\log_{10} P = \log_{10} a + b \times \log_{10} Q \quad (1)$$

where the P and Q represent the unit price and purchase quantity, respectively. And a and b are constants specific to each chemical. Consequently, the bulk price of the synthetic ZPS powder can be estimated to be 142.2 \$ kg^{-1} (Tables S1 and S2, Supporting Information), which is lower than that of many reported Zn^{2+} polymer electrolytes (Tables S3–S5, Supporting Information).^[6a,d,7,13] Furthermore, the scalable roll-to-roll fabrication method employed in this work also contributes to reducing the manufacturing process cost.

In contrast to the synthesis route reported by See et al. that involved to use Zn, P_2S_5 , and S as starting materials,^[10] a different approach was employed in this work. Here, the elemental Zn, P, and S (mol/mol/mol, 1:1:3) were sealed in an evacuated quartz tube and heated at a higher temperature of 500 °C for 8 h to produce the off-white ZPS powder. Such a high-temperature solid–liquid–vapor triphasic reaction results in the sharp and well-resolved X-ray diffraction (XRD) peaks in Figure 2a, indicating the pure phase and highly crystalline nature of the ZPS product. The refined layered ZPS crystallizes in the monoclinic C2/m (12) space group (JCPDS No. 84–0996), and the lattice parameters are $a = 5.963372$ Å, $b = 10.373396$ Å, $c = 6.746003$ Å ($\alpha = \gamma = 90.000^\circ$, $\beta = 107.094^\circ$). Furthermore, the electronic structure of ZPS was analyzed using the calculated total density of states (DOS), as shown in Figure 2b. The band gap of ZPS was determined to be 2.0 eV, which closely resembles the band gap of the insulated ZnS (2.2 eV, Figure S1, Supporting Information), indicating the electronic insulating property of ZPS. From the battery fabrication perspective, the

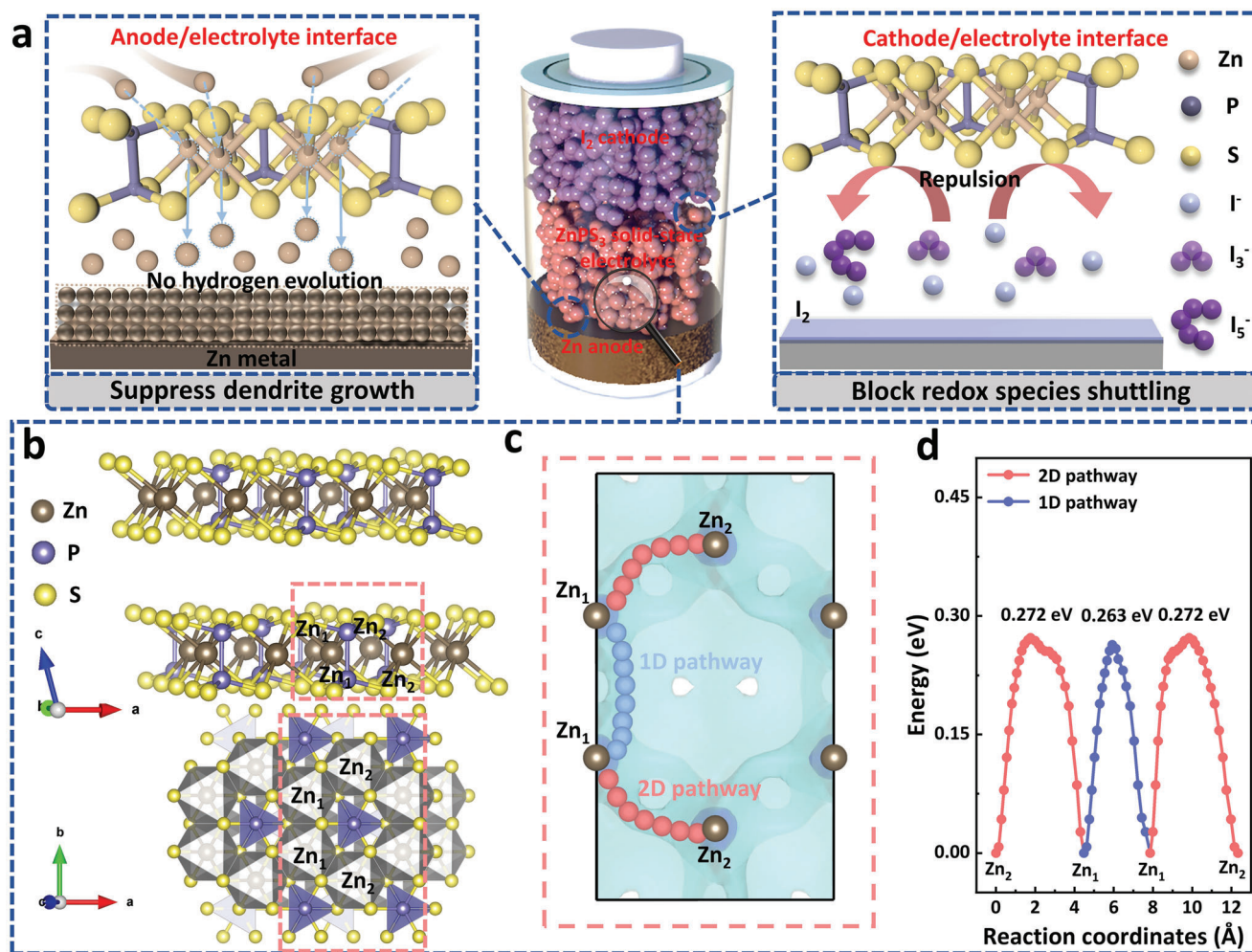


Figure 1. a) Proposed solid-state Zn–I₂ battery prototype composed of Zn metal anode, I₂ cathode, and ZnPS₃ (ZPS) electrolyte. b) Crystal structure of ZPS. c) Zn²⁺ migration paths in the crystalline framework of ZPS and d) the corresponding energy barriers.

electronic insulating property of ZPS makes it a promising candidate for achieving stable open-circuit/output voltage and long-term cycling performance in solid-state batteries.^[14]

The field emission scanning electron microscope (FESEM) image reveals agglomerated ZPS particle with a microsized scale of >10 μm (Figure 2c), and Zn, P, and S elements are uniformly distributed onto the surface. The superionic conductivity of ZPS relies on the presence of adsorbed water on its grains, making its chemical stability in water crucial for its performance. The coarse-grained ZPS sample may contribute to enhanced ion conductivity but could also be vulnerable to atmospheric humidity attacks, similar to the behavior observed in LLZO (Li–La–Zr–O).^[1b] To examine this hypothesis, a certain amount of ZPS powder was immersed in deionized water (100% humidity) for several days (Figure S2, Supporting Information). After 1 day, some pristine crystal facets of ZPS undergo distortion, which may be resulted from the structural and chemical instability of ZPS in humid air environments along with releasing a trace amount of the toxic gas of H₂S,^[1b,15] but the dominant (001) peak still maintains strong intensity. Continuing immersion for 3 and 5 days leads to a significant decline in crystallinity, and the characteristic reflections

of ZPS even vanish in the XRD results. This observation could be attributed to the transformation reaction of ZPS induced by excess water exposure.^[10b] To address this critical problem, a solution involving the combination of ZPS particles with completely hydrophobic and nonconductive PTFE is proposed, forming the flexible solid-state ZPS electrolyte, as shown in Figure 2d. The solid ZPS electrolyte membrane can be adjusted to a thickness as thin as about 119 μm (Figure S3, Supporting Information), resulting in a smooth surface.

To access the interfacial wettability, the contact angles between water and ZPS powder/membrane were measured. In Figure S4 (Supporting Information), the water can completely wet the surface of ZPS particles with a contact angle of nearly 0°, but the water droplet at the surface of ZPS membrane can only remain a hemispheric shape with a relatively larger contact angle of 69.9° (Figure S5, Supporting Information). The manipulation of surface hydrophobicity and structural integrity contributes to the improved structural stability in humid air environments, thus the ZPS membrane can retain a high crystallinity even after being immersed in deionized water for 1 month (Figure 2e and Figure S6, Supporting Information). Meanwhile, the concentration

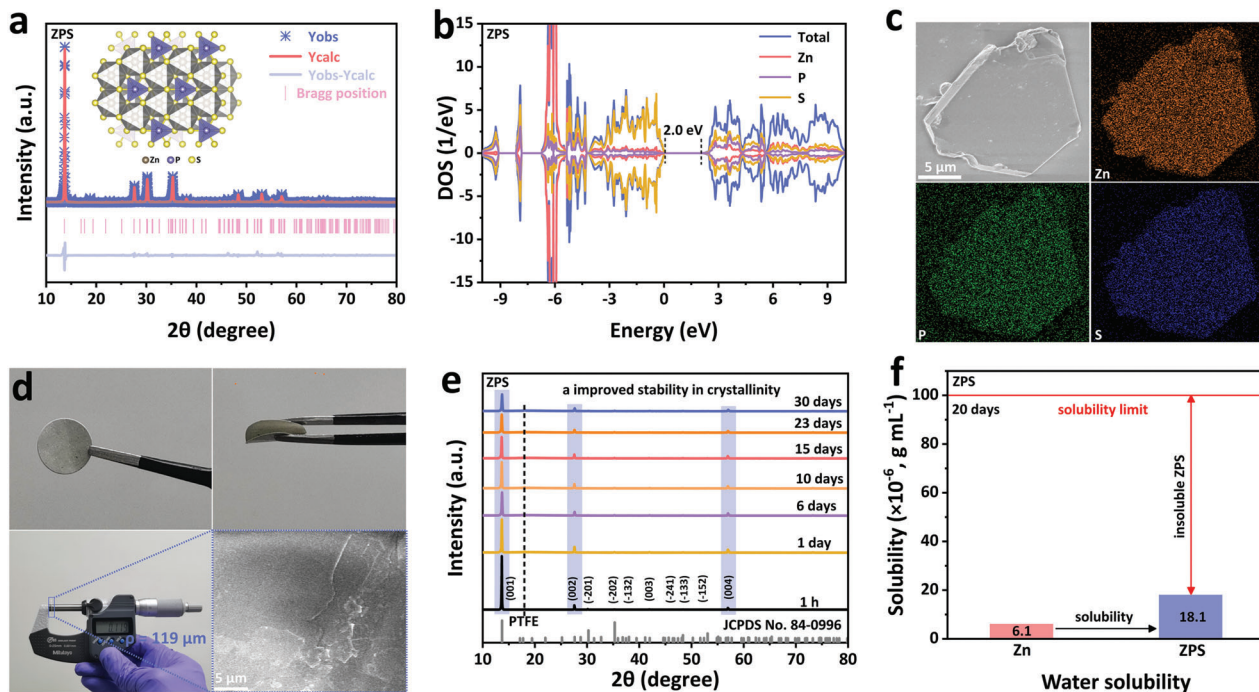


Figure 2. a) X-ray diffraction (XRD) pattern of ZnPS_3 (ZPS) with its Rietveld refinement result. b) Total density of state (DOS) of ZPS. c) Scanning electron microscope (SEM) image and elemental mappings of Zn, P, and S for ZPS. d) Optical and SEM images of ZPS electrolyte membrane. e) XRD results of ZPS membrane immersed into deionized water for long duration. f) The water solubility of ZPS presumed by the inductively coupled plasma spectrometer (ICP) result derived from immersing a piece of ZPS membrane into deionized water for 20 days.

of Zn^{2+} ions in the soaking water is also analyzed by the inductively coupled plasma spectrometer (ICP). As shown in Figure 2f, the resulted Zn^{2+} ions concentration is measured to be $6.1 \times 10^{-6} \text{ g mL}^{-1}$, corresponding to the water solubility of $18.1 \times 10^{-6} \text{ g mL}^{-1}$ for ZPS. Based on the physicochemical property, the value of insolubility for a certain material is defined as lower than $100 \times 10^{-6} \text{ g mL}^{-1}$ generally. For ZPS membrane, its water solubility is measured to be far below the solubility limit, and the pH value of the deionized water after the corresponding immersion experiment is tested to be nearly neutral (Figure S7, Supporting Information), confirming the insoluble feature and negligible H_2S gas production of ZPS membrane in water.^[10b] Furthermore, the water-stability trait of ZPS also can be validated by the Raman results (Figure S8, Supporting Information). As a member of the MPS_3 compounds, the characteristic vibration peaks of ZPS contain A_g and E_g modes, respectively.^[16] The two peaks at 226 cm^{-1} ($E_g^{(1)}$) and 279 cm^{-1} ($E_g^{(2)}$) can be assigned to the tangential vibration of the P–P bond and the in-plane vibrations of the $[\text{P}_2\text{S}_6]^{4-}$ poly anion, respectively, and the other peaks at 259 cm^{-1} ($A_{1g}^{(1)}$) and 388 cm^{-1} ($A_{1g}^{(2)}$) represent the stretching vibration of the P–P bond and the out-of plane vibrations of the $[\text{P}_2\text{S}_6]^{4-}$ unit, respectively. Clearly, Raman characteristic peaks of ZPS electrolyte remain unchanged after being immersed into deionized water for a month (Figure S8, Supporting Information). In summary, the comprehensive material characterizations demonstrate the significant advantages of the ZPS electrolyte, including electronic insulation, good structural integrity, and high stability in water. These exceptional properties make the ZPS electrolyte highly suitable for meeting the critical requirements in battery implementation.

The Zn^{2+} conducting behavior of ZPS electrolyte was investigated by both experimental and theoretical calculation approaches. Firstly, the room-temperature ion conductivity of ZPS is measured to be $9.3 \times 10^{-9} \text{ S cm}^{-1}$, which is lower than the previous reported value of 10^{-8} – $10^{-6} \text{ S cm}^{-1}$ at 60°C owing to the addition of nonconductive PTFE (Figure S9, Supporting Information).^[10a] Encouragingly, the superionic conductive capability of ZPS can be activated by combining with crystalline water, and the subsequent ion conductivity of ZPS is improved about several orders of magnitude.^[10b] In our work, the ZPS electrolyte is immersed into deionized water for 1 h to establish the spontaneous water adsorption of ZPS and reduce the electrolyte/electrode contact resistance. Afterward, the residual free water on the surface of ZPS is carefully removed by air-laid paper and the resultant hydrated ZPS is characterized through Fourier transform infrared (FT-IR), ^1H magic angle spinning nuclear magnetic resonance (NMR), thermal gravimetric analysis (TGA), and differential scanning calorimetry (DSC) (Figures S10–S12). The comprehensive analysis results show that the H bond network of water molecules is interrupted by ZPS crystalline host and the existing low content of absorbed water ($0.13 \text{ H}_2\text{O}/\text{ZPS}$, mol/mol) should be closely bound to ZPS grains.

Then, the ZPS electrolyte was sandwiched between two stainless steels plates to measure ionic conductivities ranging from 30°C to 80°C (Figure 3a and Figure S13, Supporting Information). Encouragingly, the obtained ion conductivity of $2.0 \times 10^{-3} \text{ S cm}^{-1}$ at 30°C is higher than that of many other reported polymer electrolytes for ZIBs (Figure 3c).^[6b-e,7] And the corresponding Zn^{2+} migration barrier in the bulk ZPS (Figure 3b) can be estimated to be 33.6 kJ mol^{-1} according to the Arrhenius equation.

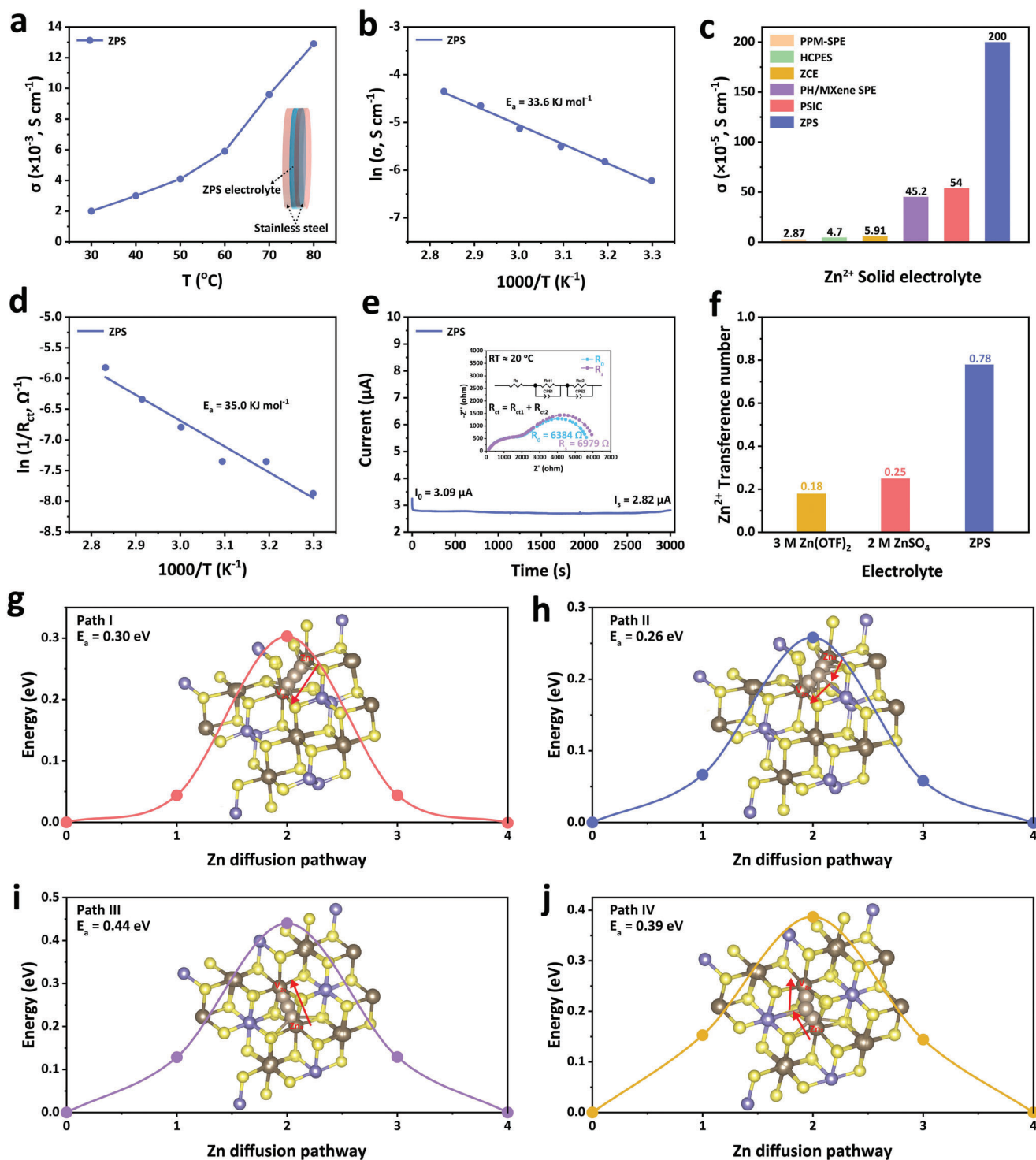


Figure 3. a) The temperature-dependent ion conductivities of ZnPS $_3$ (ZPS) from 30 $^{\circ}$ C to 80 $^{\circ}$ C. b) Arrhenius plots of the ionic conductivity for ZPS. c) The comparisons of ion conductivities between ZPS electrolyte and other Zn $^{2+}$ solid polymer electrolytes (SPEs). d) The total energy barrier of mass and charge transfer processes in solid-state Zn||Zn symmetric cell with ZPS electrolyte. e) Current variations of the Zn||Zn with ZPS electrolyte at room temperature with potentiostatic polarization ($\Delta V = 20$ mV), the inset shows the EIS before and after polarization. f) The comparisons of Zn $^{2+}$ transference number between ZPS and liquid electrolytes. g–j) The four possible Zn $^{2+}$ migration paths with vacancy-hopping mechanism in crystalline ZPS host.

Furthermore, the solid-state Zn||Zn symmetrical cells were also assembled to take into account both mass and charge transfer processes (Figures S14 and S15, and Table S6, Supporting Information), and the corresponding energy barrier is calculated to be about 35.0 kJ mol⁻¹ (Figure 3d). The almost negligible energy barrier difference ($\Delta = 1.4$ kJ mol⁻¹) may imply the intrinsic nondesolvation mechanism of solid-state ZPS electrolyte. Additionally, the Zn²⁺ transference number ($t_{\text{Zn}^{2+}}$) of ZPS was figured out via the time-dependence of 20 mV-potentiostatic DC (direct-current) polarization test (Figure 3e). In comparison to commonly used liquid electrolytes including 3 M Zn(CF₃SO₃)₂ (Zn(OTF)₂) ($t_{\text{Zn}^{2+}} = 0.18$) and 2 M ZnSO₄ ($t_{\text{Zn}^{2+}} = 0.25$) (Figures S16 and S17, Supporting Information), the higher $t_{\text{Zn}^{2+}}$ of ZPS ($t_{\text{Zn}^{2+}} = 0.78$) contributes to higher cationic selectivity and suppressed side reactions in solid-state batteries (Figure 3f). Thus, the Zn²⁺ ions conductivity ($\sigma_{\text{Zn}^{2+}}$) of ZPS can be calculated as 1.56×10^{-3} S cm⁻¹ according to the following Equation (2), which exceeds many reported polymer-based solid-state electrolytes in ZIBs (Table S7, Supporting Information).^[6b-e,17]

$$\sigma_{\text{Zn}^{2+}} = \sigma \times t_{\text{Zn}^{2+}} \quad (2)$$

Moreover, the evidences of Zn²⁺ mobility in ZPS are also accessed by density functional theory (DFT) calculations. Similar to the reported vacancy hopping mechanism,^[10a] a charge neutral Zn vacancy (V_{Zn}) is constructed to study the Zn²⁺ migration processes in ZPS (Figure 3g–j). The two symmetric Zn sites distribute at either side of V_{Zn} are labeled as Zn₁, and the other Zn site locate under the V_{Zn} is labeled as Zn₂. Taking the V_{Zn} as a destined migration site, it can be concluded that there are two diffusion types including (1) Zn²⁺ directly moves along a straight line with a 1D pathway toward the V_{Zn} (paths I and III) and (2) Zn²⁺ passes through the face of Zn octahedra along the Zn–S coordination sites with a 2D pathway (paths II and IV), which corroborates the BVSE results. And the associated low energy barriers are calculated to be 0.30, 0.26, 0.44, and 0.39 eV for paths I–IV, respectively, which are close to the above experimental value of 33.6 kJ mol⁻¹ (0.35 eV).

The compatibility between the solid-state ZPS electrolyte and Zn metal anode is further evaluated by assembling Zn||Zn symmetrical cells. As shown in **Figure 4a**, the Zn||Zn symmetrical cell using the ZPS electrolyte can maintain a stable cycling up to 400 h at 0.1 mAh cm⁻² and 0.1 mA cm⁻², revealing the good interface stability. To ascertain the structural stability of ZPS electrolyte during cycling, the in situ Laser Raman spectrum detection was conducted under the initial cycle of Zn||Zn symmetrical cell. During the Zn plating/stripping processes, four characteristic vibration peaks are detected to be consistent without obvious shift, reflecting the reliable electrochemical stability of ZPS (Figure 4b). Especially, the significant enhanced vibration intensities of E_g⁽²⁾ and A_g⁽²⁾ modes may could be attributed to the activation process of Zn²⁺ migration sites in crystalline ZPS during electrochemical cycling. Moreover, the ZPS tend to be a single ion conductor that can provide fast ion diffusion paths to redistribute the Zn²⁺ flux prominently, leading to uniform Zn deposition. After 10 cycles in 2 M ZnSO₄ liquid electrolyte, the Zn dendrites in the form of vertical nanosheets can be observed in Figure S18 (Supporting Information), and the XRD results also corroborates the formation of detrimental Zn₄SO₄(OH)₆·xH₂O

by-products (Figure S19, Supporting Information). However, the smooth Zn²⁺ deposition morphology without the formation of Zn₄SO₄(OH)₆·xH₂O in ZPS can be achieved (Figures S20 and S21, Supporting Information). More apparent differences can be observed in atomic force microscope (AFM) images (Figure 4c,d), which implies the ZPS electrolyte can suppress the Zn dendrite formation and facilitate the uniform Zn²⁺ deposition. .

The deposition morphology may be determined by the crystal orientation, which can be accessed by the grazing incidence X-ray diffraction (GIXRD). As shown in Figure 4e, GIXRD patterns of the deposited Zn with 10 h plating show the higher $I_{(002)}/I_{(100)}$ value of 1.66 with solid Zn²⁺ transportation, illustrating the preferential orientation of a (002) plane during the Zn²⁺ plating process with ZPS.^[4a,18] From a fundamental view, the orientation of deposited crystal facets is closely associated with the reaction interface. In sulfide solid-state lithium-ion batteries with Li₁₀GeP₂S₁₂ (LGPS) electrolyte, it is generally recognized that there is a spontaneous decomposition reactions occurring at the interface between solid electrolyte and lithium metal, resulting in the formation of a mixture composed of Li₂S, Li₃P, and Li–Ge alloy.^[19] Therefore, it is reasonable to predict the possible formation of ZnS at the Zn/ZPS interface during cycling, which has been demonstrated to be capable of enhancing the reversibility of Zn metal anode.^[20] In Figure 4f, X-ray photoelectron spectrometer (XPS) was carried out to detect Zn electrode surfaces in both 2 M ZnSO₄ and ZPS after five cycles. The S 2p spectrum displays the co-existence of SO₃²⁻ and SO₄²⁻ anions on the Zn surface cycled in 2 M ZnSO₄, which could be attributed to the hydrous hydroxide Zn₄SO₄(OH)₆·xH₂O.^[21] While the characteristic peak separation of 1.2 eV in the deconvolution of the S 2p spectrum for Zn electrode in ZPS represents the existence of bivalent S²⁻, corresponding to the ZnS layer potentially.^[21,22]

Based on the previous research,^[20,23] the transformation of the Zn(002) facet into ZnS (002) is thermodynamically favored when the Zn metal comes into contact with a sulfurous atmosphere. The unbalanced charge distribution at the Zn(002)-ZnS(002) interface, caused by the strong bonding interaction between the S atoms in ZnS and the Zn atoms in Zn metal, promotes the Zn²⁺ diffusion and guides uniform Zn plating/stripping (Figure S22, Supporting Information).^[20] Therefore, the multi-interface compatibility is investigated (Figure 4g), and the binding energy of $E_{\text{Zn}(002)\text{-ZPS}(002)}$, $E_{\text{Zn}(002)\text{-ZnS}(002)}$, and $E_{\text{ZnS}(002)\text{-ZPS}(002)}$ are found to be -0.08, -0.05, and -0.07 eV, respectively. Negative values of interface energy indicate preferring chemical affinity, but moderated interfacial interaction facilitates free Zn²⁺ diffusion.^[4a] Therefore, the tendency of $E_{\text{Zn}(002)\text{-ZPS}(002)} < E_{\text{ZnS}(002)\text{-ZPS}(002)} < E_{\text{Zn}(002)\text{-ZnS}(002)}$ suggests improved Zn²⁺ diffusion kinetics and the interfacial thermodynamical stability. Furthermore, the possibility of Zn²⁺ migration along the ZnS(002) facet is studied by placing a lone Zn²⁺ ion onto the surface of different ZnS facets (Figure 4h). The Zn²⁺ ion is irreversibly trapped at ZnS(110) with the huge binding force derived from the Zn²⁺ and ZnS(110) ($E_{\text{Zn-ZnS}(110)} = -13.49$ eV), and the ZnS(100) is slightly distorted by the weak adsorption effect resulting from the alien Zn²⁺ ($E_{\text{Zn-ZnS}(100)} = -0.14$ eV). However, the positive value of $E_{\text{Zn-ZnS}(002)}$ (1.09 eV) reveals negligible chemical affinity between Zn²⁺ and ZnS(002). In addition, compared with the high-resistance Zn²⁺ diffusion in bulk ZnS (-0.23 eV), the extremely low barrier of 0.03 eV for Zn²⁺ diffusion along ZnS (002)

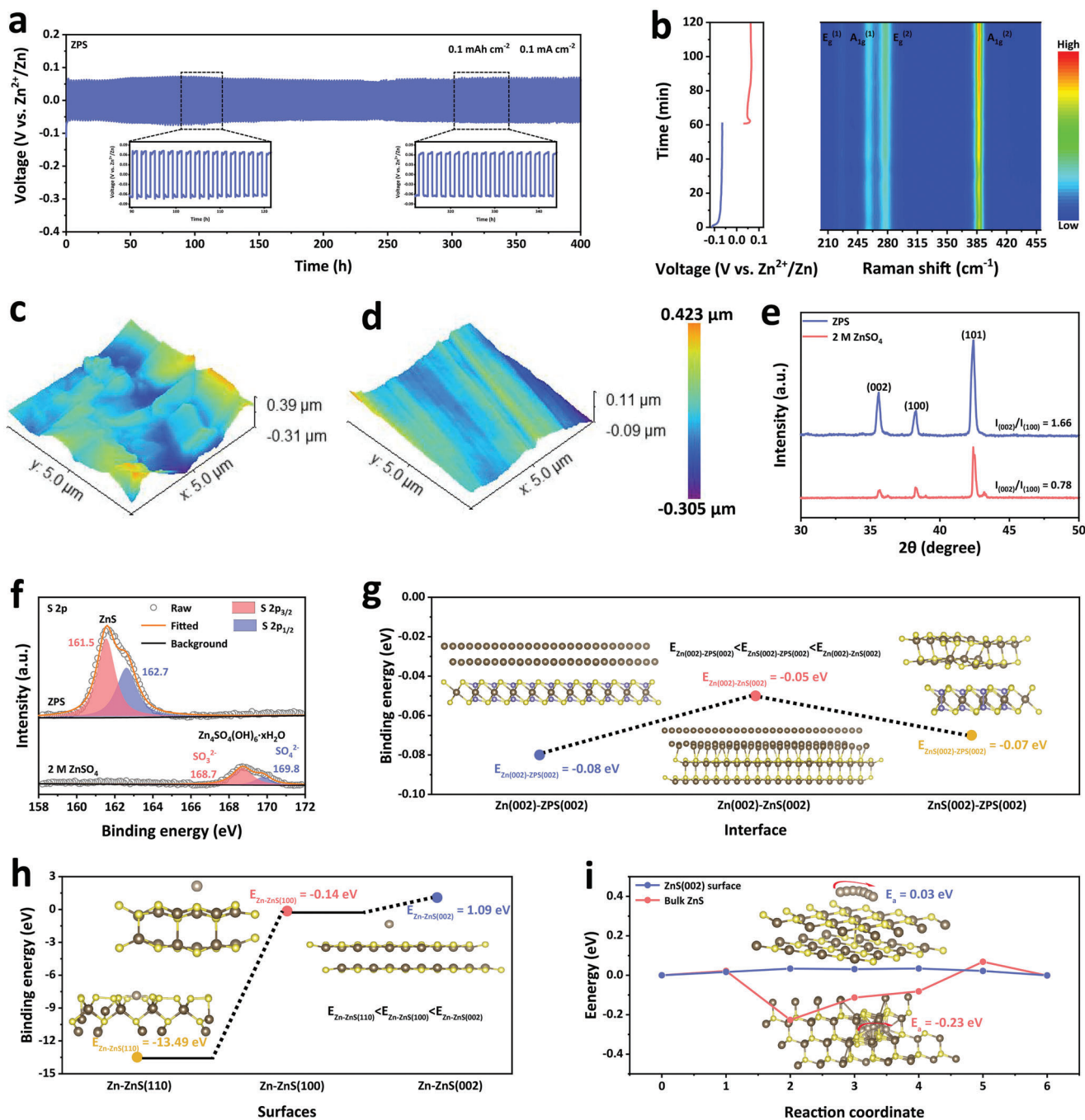


Figure 4. a) Galvanostatic Zn^{2+} plating/stripping in $\text{Zn}||\text{Zn}$ symmetric cells with ZnPS_3 (ZPS) electrolyte at 0.1 mA cm^{-2} with 0.1 mAh cm^{-2} capacity. b) In situ Raman results of $\text{Zn}||\text{Zn}$ with ZPS electrolyte at initial cycle. Atomic force microscope (AFM) images of Zn electrodes after 10 cycles in c) 2 M ZnSO_4 and d) ZPS electrolytes. e) Grazing incidence X-ray diffraction (GIXRD) patterns of plating Zn^{2+} on Zn foil for 10 h with 2 M ZnSO_4 and ZPS electrolytes. f) S 2p X-ray photoelectron spectrometer (XPS) spectra of Zn electrodes after five cycles in 2 M ZnSO_4 and ZPS electrolytes. g) The calculated interfacial energies of Zn(002)-ZPS(002), Zn(002)-ZnS(002), and ZnS(002)-ZPS(002). h) The binding energies of Zn-ZnS(110), Zn-ZnS(100), and Zn-ZnS(002). i) The barriers for Zn^{2+} diffusion along ZnS(002) surface and in the bulk ZnS.

indicates the preferential ZnS(002) plane diffusion of the released Zn^{2+} (Figure 4i). In summary, the high Zn/ZnS/ZPS interfacial compatibility and the underlying multi-interface Zn^{2+} transfer mechanism may suggest that the fabrication of solid-state Zn-I_2 batteries with ZPS electrolyte and Zn metal anode

is feasible, offering potential benefits in Zn^{2+} diffusion kinetics and deposition behavior.

In the evaluation of ZPS electrolyte in a full battery with a Zn metal anode and a halide I_2 cathode, the as-fabricated solid-state $\text{Zn}||\text{I}_2@AC$ full cell shows 225.2, 168.7, and 86.2 mAh g^{-1} at 0.1,

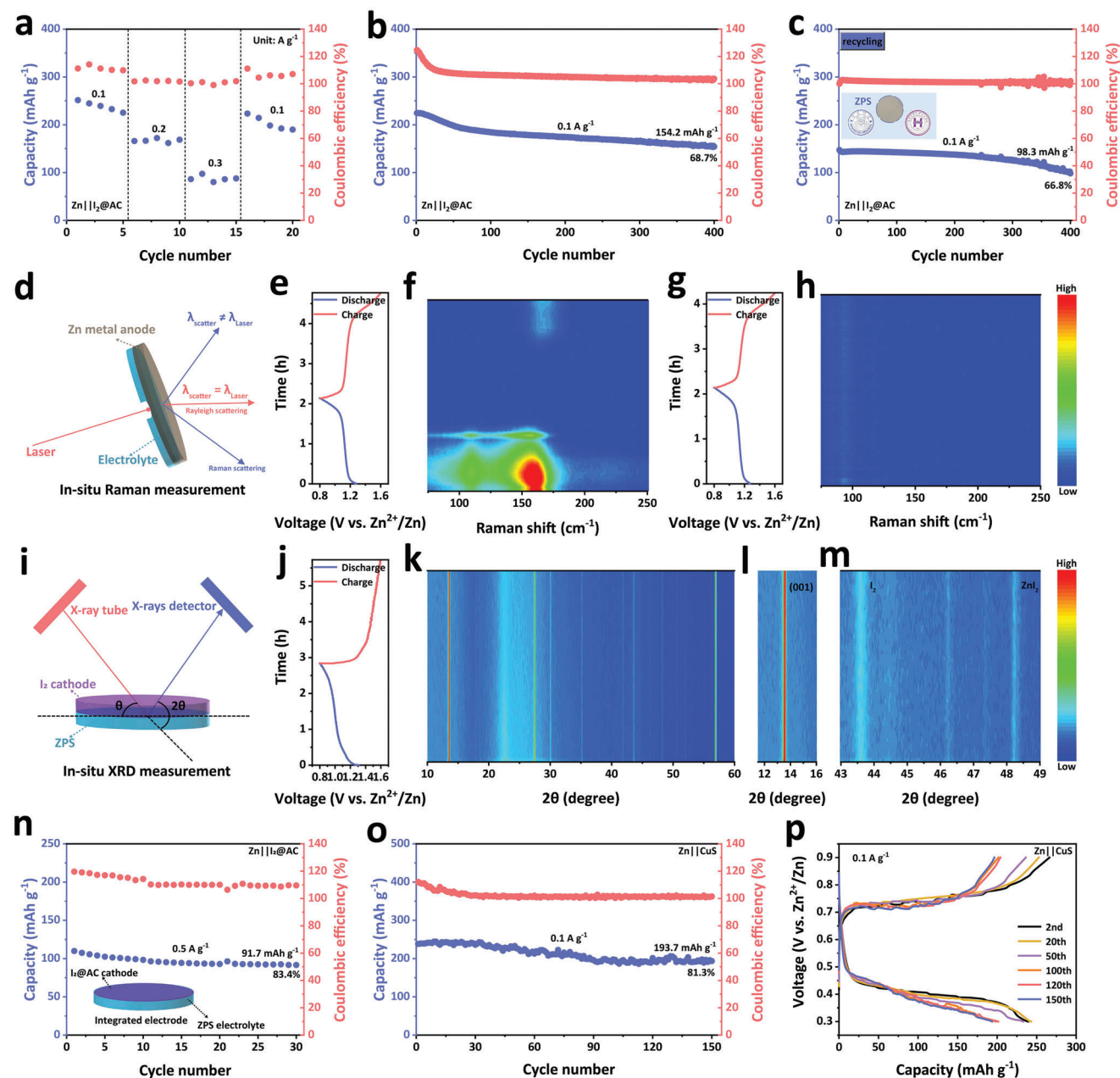


Figure 5. a) Rate performance of Zn||I₂@AC. Cycling performances of b) Zn||I₂@AC with fresh ZnPS₃ (ZPS) electrolyte and c) the recycled Zn||I₂@AC with the recyclable ZPS. Simple schematic diagrams of d) in situ Raman and i) in situ X-ray diffraction (XRD) measurements. The in situ Raman results of Zn||I₂@AC in f) 2 M ZnSO₄ and h) ZPS electrolytes, and e, g) the corresponding initial discharge–charge profiles of Zn||I₂@AC with ZPS electrolyte and k–m) the corresponding results for in situ XRD measurement. n) The high-rate performance of solid-state Zn||I₂@AC with the integrated electrode. o) The cycling stability of Zn||CuS with ZPS electrolyte at 0.1 A g⁻¹ and p) the corresponding discharge–charge curves.

0.2, and 0.3 A g⁻¹ (Figure 5a), respectively, and it even exhibits an impressive reversible capacity of 154.2 mAh g⁻¹ after 400 cycles at 0.1 A g⁻¹ (Figure 5b and Figure S23, Supporting Information), such a relatively stable low-rate cycling performance is almost comparable to that of the previous reports about zinc–iodine batteries (Table S8, Supporting Information).^[24] Remarkably, the ZPS electrolyte membrane remained intact even after cycling, displaying a smooth surface and excellent structural integrity (insert in Figure 5c). Interestingly, the Zn||I₂@AC battery

with the ZPS electrolyte recycled from disassembled batteries also displays a stable cycling performance with a high-capacity retention of 66.8% for 400 cycles (Figure S24, Supporting Information), reinforcing the unique advantages of high structural stability and durable Zn²⁺ conductive capability for ZPS. It is worth noting that the recycled Zn||I₂@AC does not show Coulombic efficiency anomalies, which may be attributed to the suppressed polyiodide species dynamic migration resulted from a certain amount of iodine ions having fully filled the pores or microcracks

(Figure S3, Supporting Information, the SEM image of the cross-section of the ZPS electrolyte) in the recycled ZPS membrane.^[25] In conventional liquid electrolytes, the accumulation and shuttle of soluble polyiodide species can cause capacity decay and poor reversibility.^[3,24a-c] However, the solid-state Zn||I₂ battery with ZPS electrolyte contributes to suppressing these issues, as confirmed by in situ Raman measurements on the Zn/electrolyte interface (Figure 5d). In contrast to the visible Raman peaks of I₃⁻ (≈110 cm⁻¹) and I₅⁻ (≈160 cm⁻¹) during the initial cycle in liquid 2 M ZnSO₄ electrolyte (Figure 5e,f), the polyiodide shuttle is effectively suppressed in the solid Zn-I₂ battery (Figure 5g,h) due to the blocking effect of the solid-state ZPS electrolyte. To gain deeper insight into the redox reaction occurring at the I₂/ZPS interface, in situ XRD was also employed (Figure 5i). The high-resolution XRD spectra (Figure 5k,l) show that the electrochemically stable ZPS electrolyte exhibits constant peak positions and crystal orientation, facilitating the durative Zn²⁺ transportation in ZPS and ensuring long-term cycling stability for the Zn-I₂ system. Additionally, the peaks at ≈43.5° and ≈48.1° could be attributed to I₈ (JCPDS No. 96-451-1286) and ZnI₂ (JCPDS No. 70-1224), respectively, corresponding to the dominant I⁻/I⁰ redox couples in solid-state Zn-I₂ system (Figure 5m).

In order to further improve the volumetric energy density of the solid-state Zn-I₂ full cell, a novel integrated electrode was designed by directly coating the I₂@AC slurry on the surface of ZPS (Figure 5n). Surprisingly, the total mass of the integrated electrolyte/cathode is only about one-third of the conventional glass fiber separator loaded with 120 μL liquid electrolyte (Table S9, Supporting Information), and the compact contact of electrode and electrolyte in the integrated electrode can lower the contact resistance of solid-solid electrode/electrolyte interface, thus, the integrated electrode can still maintain 83.4% of the initial capacity at a high rate of 0.5 A g⁻¹ after 30 cycles. This result highlights the significant potential for increasing the energy density of Zn-I₂ batteries by utilizing the integrated electrode design. Moreover, the electrode compatibility of the ZPS electrolyte was further demonstrated in the combination of a CuS cathode. As depicted in Figure 5o,p, the Zn||CuS full cell displays a stable cycling performance over 150 cycles and maintains a sustained output voltage of approximately 0.4 V. This emphasizes the wide applicability of the solid-state ZPS electrolyte for other Zn metal battery systems, showcasing its versatility and potential for use in various battery configurations.

3. Conclusion

In this work, the inorganic solid-state ZPS electrolyte with high ion conductivity, facilitated Zn²⁺ ion migration and excellent chemical/electrochemical stability is employed for the successful fabrication of Zn-I₂ batteries. The high Zn²⁺ transference number and nondesolvation solid Zn²⁺ ion conductive mechanism of ZPS endow Zn metal anode with the advantages of suppressed Zn dendrite growth and preferential Zn(002) deposition orientation. The in situ Raman and XRD results further confirm the effective blocking of polyiodide shuttling, ensuring the predominant conversion of I⁻/I⁰ redox couple, which is crucial for enhancing the electrochemical stability. Consequently, the successful application of Zn||I₂@AC and Zn||CuS full cells demonstrates the immense potential of the ZPS electrolyte as a promis-

ing inorganic solid-state Zn²⁺ ion conductor, which opens up new possibilities for developing practical solid-state Zn-based batteries using inorganic crystalline electrolytes.

Supporting Information

Supporting Information is available from the Wiley Online Library or from the author.

Acknowledgements

The authors gratefully acknowledge the financial support from National Natural Science Foundation of China (No. 22109030 and 22021001), Fundamental Research Funds for the Central Universities (20720220073), the Key Research and Development Program of Yunnan Province (202103AA080019), and Fujian Industrial Technology Development and Application Plan (202210002). The numerical calculations in this paper have been done on Hefei advanced computing center.

Conflict of Interest

The authors declare no conflict of interest.

Data Availability Statement

The data that support the findings of this study are available from the corresponding author upon reasonable request.

Keywords

inorganic solid-state Zn-I₂ batteries, solid-state Zn²⁺ conduction, Zn metal anodes, ZnPS₃

Received: August 31, 2023

Revised: September 21, 2023

Published online:

- [1] a) T. Ma, Z. Wang, D. Wu, P. Lu, X. Zhu, M. Yang, J. Peng, L. Chen, H. Li, F. Wu, *Energy Environ. Sci.* **2023**, *16*, 2142; b) M. Nasir, J. Y. Park, P. Heo, K. H. Choi, H. J. Park, *Adv. Funct. Mater.* **2023**, *33*, 2303397; c) Y. C. Yin, J. T. Yang, J. D. Luo, G. X. Lu, Z. Huang, J. P. Wang, P. Li, F. Li, Y. C. Wu, T. Tian, Y. F. Meng, H. S. Mo, Y. H. Song, J. N. Yang, L. Z. Feng, T. Ma, W. Wen, K. Gong, L. J. Wang, H. X. Ju, Y. Xiao, Z. Li, X. Tao, H. B. Yao, *Nature* **2023**, *616*, 77.
- [2] a) L. Wang, Z. Wang, H. Li, D. Han, X. Li, F. Wang, J. Gao, C. Geng, Z. Zhang, C. Cui, Z. Weng, C. Yang, K. P. Loh, Q. H. Yang, *ACS Nano* **2023**, *17*, 668; b) Z. Meng, Y. Jiao, P. Wu, *Angew. Chem. Int. Ed.* **2023**, *62*, e202307271; c) W. Liu, Q. Zhao, H. Yu, H. Wang, S. Huang, L. Zhou, W. Wei, Q. Zhang, X. Ji, Y. Chen, L. Chen, *Adv. Funct. Mater.* **2023**, *33*, 2302661; d) F. Ling, L. Wang, F. Liu, M. Ma, S. Zhang, X. Rui, Y. Shao, Y. Yang, S. He, H. Pan, X. Wu, Y. Yao, Y. Yu, *Adv. Mater.* **2023**, *35*, 2208764; e) S. Zheng, L. Wei, Z. Zhang, J. Pan, J. He, L. Gao, C. C. Li, *Nano Lett.* **2022**, *22*, 9062; f) J. Ke, Z. Wen, Y. Yang, R. Tang, Y. Tang, M. Ye, X. Liu, Y. Zhang, C. C. Li, *Adv. Funct. Mater.* **2023**, *33*, 2301129; g) S. Li, C. Huang, L. Gao, Q. Shen, P. Li, X. Qu, L. Jiao, Y. Liu, *Angew. Chem. Int. Ed.* **2022**, *61*, e202211478; h) M. Liu, W. Yuan, G. Ma, K. Qiu, X. Nie, Y. Liu, S. Shen, N. Zhang, *Angew. Chem. Int. Ed.* **2023**, *62*, e202304444.

- [3] a) Y. Yang, S. Liang, B. Lu, J. Zhou, *Energy Environ. Sci.* **2022**, *15*, 1192; b) Z. Li, X. Wu, X. Yu, S. Zhou, Y. Qiao, H. Zhou, S. G. Sun, *Nano Lett.* **2022**, *22*, 2538.
- [4] a) Y. Zhang, X. Li, L. Fan, Y. Shuai, N. Zhang, *Cell Rep Phys Sci* **2022**, *3*, 100824; b) Y. Song, P. Ruan, C. Mao, Y. Chang, L. Wang, L. Dai, P. Zhou, B. Lu, J. Zhou, Z. He, *Nano-Micro Lett.* **2022**, *14*, 218; c) L. Lin, Z. Lin, J. Zhu, K. Wang, W. Wu, T. Qiu, X. Sun, *Energy Environ. Sci.* **2023**, *16*, 89.
- [5] Y. Ma, J. Wan, X. Xu, A. D. Sendek, S. E. Holmes, B. Ransom, Z. Jiang, P. Zhang, X. Xiao, W. Zhang, R. Xu, F. Liu, Y. Ye, E. Kaeli, E. J. Reed, W. C. Chueh, Y. Cui, *ACS Energy Lett.* **2023**, *8*, 2762.
- [6] a) L. Ma, S. Chen, N. Li, Z. Liu, Z. Tang, J. A. Zapien, S. Chen, J. Fan, C. Zhi, *Adv. Mater.* **2020**, *32*, 1908121; b) Z. Zhao, J. Wang, Z. Lv, Q. Wang, Y. Zhang, G. Lu, J. Zhao, G. Cui, *Chem. Eng. J.* **2021**, *417*, 128096; c) Z. Chen, T. Wang, Y. Hou, Y. Wang, Z. Huang, H. Cui, J. Fan, Z. Pei, C. Zhi, *Adv. Mater.* **2022**, *34*, 2207682; d) J. Feng, D. Ma, K. Ouyang, M. Yang, Y. Wang, J. Qiu, T. Chen, J. Zhao, B. Yong, Y. Xie, H. Mi, L. Sun, C. He, P. Zhang, *Adv. Funct. Mater.* **2022**, *32*, 2207909; e) G. Lu, H. Qiu, X. Du, K. K. Sonigara, J. Wang, Y. Zhang, Z. Chen, L. Chen, Y. Ren, Z. Zhao, J. Du, S. Li, J. Zhao, G. Cui, *Chem. Mater.* **2022**, *34*, 8975.
- [7] H. Qiu, R. Hu, X. Du, Z. Chen, J. Zhao, G. Lu, M. Jiang, Q. Kong, Y. Yan, J. Du, X. Zhou, G. Cui, *Angew. Chem. Int. Ed.* **2022**, *61*, e202113086.
- [8] L. Ma, S. Chen, X. Li, A. Chen, B. Dong, C. Zhi, *Angew. Chem. Int. Ed.* **2020**, *59*, 23836.
- [9] Z. Guo, T. Wang, H. Wei, Y. Long, C. Yang, D. Wang, J. Lang, K. Huang, N. Hussain, C. Song, B. Guan, B. Ge, Q. Zhang, H. Wu, *Angew. Chem., Int. Ed.* **2019**, *58*, 12569.
- [10] a) A. J. Martinolich, C.-W. Lee, I. T. Lu, S. C. Bevilacqua, M. B. Preefer, M. Bernardi, A. Schleife, K. A. See, *Chem. Mater.* **2019**, *31*, 3652; b) Z. W. B. Iton, B. C. Lee, A. Y. Jiang, S. S. Kim, M. J. Brady, S. Shaker, K. A. See, *J. Am. Chem. Soc.* **2023**, *145*, 13312.
- [11] a) H. Chen, L. L. Wong, S. Adams, *Acta Cryst.* **2019**, *B75*, 18; b) L. L. Wong, K. C. Phuah, R. Dai, H. Chen, W. S. Chew, S. Adams, *Chem. Mater.* **2021**, *33*, 625.
- [12] K. Wang, Q. Ren, Z. Gu, C. Duan, J. Wang, F. Zhu, Y. Fu, J. Hao, J. Zhu, L. He, C. W. Wang, Y. Lu, J. Ma, C. Ma, *Nat. Commun.* **2021**, *12*, 4410.
- [13] M. Wang, A. Emre, S. Tung, A. Gerber, D. Wang, Y. Huang, V. Cecen, N. A. Kotov, *ACS Nano* **2019**, *13*, 1107.
- [14] S. H. Hwang, S. D. Seo, D. W. Kim, *Adv. Sci.* **2023**, *10*, 2301707.
- [15] a) S. Wang, Y. Wu, T. Ma, L. Chen, H. Li, F. Wu, *ACS Nano* **2022**, *16*, 16158; b) Y. Jin, Q. He, G. Liu, Z. Gu, M. Wu, T. Sun, Z. Zhang, L. Huang, X. Yao, *Adv. Mater.* **2023**, *35*, 2211047; c) C. Wang, K. Aoyagi, P. Wisesa, T. Mueller, *Chem. Mater.* **2020**, *32*, 3741; d) P. Lu, Y. Xia, G. Sun, D. Wu, S. Wu, W. Yan, X. Zhu, J. Lu, Q. Niu, S. Shi, Z. Sha, L. Chen, H. Li, F. Wu, *Nat. Commun.* **2023**, *14*, 4077.
- [16] a) Q. Zhang, Q. Guo, Q. Chen, X. Zhao, S. J. Pennycook, H. Chen, *Adv. Sci.* **2020**, *7*, 1902576; b) Z. Cheng, T. A. Shifa, F. Wang, Y. Gao, P. He, K. Zhang, C. Jiang, Q. Liu, J. He, *Adv. Mater.* **2018**, *30*, 1707433.
- [17] H. Qiu, R. Hu, X. Du, Z. Chen, J. Zhao, G. Lu, M. Jiang, Q. Kong, Y. Yan, J. Du, X. Zhou, G. Cui, *Angew. Chem. Int. Ed.* **2021**, *61*, e202113086.
- [18] a) Q. Zhang, J. Luan, X. Huang, Q. Wang, D. Sun, Y. Tang, X. Ji, H. Wang, *Nat. Commun.* **2020**, *11*, 3961; b) X. Yu, Z. Li, X. Wu, H. Zhang, Q. Zhao, H. Liang, H. Wang, D. Chao, F. Wang, Y. Qiao, H. Zhou, S.-G. Sun, *Joule* **2023**, *7*, 1145.
- [19] D. H. S. Tan, A. Banerjee, Z. Chen, Y. S. Meng, *Nat. Nanotechnol.* **2020**, *15*, 170.
- [20] J. Hao, B. Li, X. Li, X. Zeng, S. Zhang, F. Yang, S. Liu, D. Li, C. Wu, Z. Guo, *Adv. Mater.* **2020**, *32*, 2003021.
- [21] C. Huang, X. Zhao, S. Liu, Y. Hao, Q. Tang, A. Hu, Z. Liu, X. Chen, *Adv. Mater.* **2021**, *33*, 2100445.
- [22] L. Dai, C. Strelow, T. Kipp, A. Mews, I. Benkenstein, D. Eifler, T. H. Vuong, J. Rabeah, J. McGettrick, R. Lesyuk, C. Klinke, *Chem. Mater.* **2020**, *33*, 275.
- [23] Q. Li, C. Wang, *Appl. Phys. Lett.* **2003**, *82*, 1398.
- [24] a) H. Pan, B. Li, D. Mei, Z. Nie, Y. Shao, G. Li, X. S. Li, K. S. Han, K. T. Mueller, V. Sprenkle, J. Liu, *ACS Energy Lett.* **2017**, *2*, 2674; b) H. Yang, Y. Qiao, Z. Chang, H. Deng, P. He, H. Zhou, *Adv. Mater.* **2020**, *32*, 2004240; c) K. K. Sonigara, J. Zhao, H. K. Machhi, G. Cui, S. S. Soni, *Adv. Energy Mater.* **2020**, *10*, 2001997; d) J. Hao, L. Yuan, Y. Zhu, X. Bai, C. Ye, Y. Jiao, S. Z. Qiao, *Angew. Chem., Int. Ed.* **2023**, *62*, e202310284; e) Y. Yang, S. Guo, Y. Pan, B. Lu, S. Liang, J. Zhou, *Energy Environ. Sci.* **2023**, *16*, 2358.
- [25] K. B. Hatzell, M. Yusuf, *Nature* **2023**, *618*, 247.